

Full length article

An efficient autofocus method for microscope based on the improved first-order derivative Gaussian filtering operator[☆]

Yongxing Zhang^a, Zhenxing Shi^a, Huiquan Wang^{a,*}, Jie Pang^b

^a School of Aeronautics and Astronautics, Yuquan Campus, Zhejiang University, Hangzhou, 310027, Zhejiang, China

^b Nokia Solutions and Networks System Technology(Beijing) Co., Ltd, Beijing, 314051, Beijing, China

ARTICLE INFO

Keywords:

Edge estimation

Autofocus

Microscope

ABSTRACT

This paper introduces an improved filtering operator based on the first-order derivative Gaussian filtering operator. As the defocus distance decreases, the edges of an image transition from being smooth to sharp. Using the operator proposed in this study, a parameter can be obtained to quantify the degree of edge sharpness, where a smaller value indicates sharper edges. By using the characteristic, we can judge whether the object is near the focal plane. Combining this information, we proposed two focus method. Both of them can avoid the problem of the hill climbing algorithm locating at local extremum points and one of them can locate the watershed between “coarse search” and “fine search” before the sharpness value crosses the peak value, so as to realize the transition from “coarse search” to “fine search” before crossing the peak value and improve focusing efficiency. This is different from previous passive focusing strategies. The final experiment shows that the proposed solutions in this paper is effective. However, the methods proposed in this study are only applicable to incoherent optical microscopy imaging systems and are not suitable for coherent light source microscopy imaging systems. Besides, the prerequisite for the successful implementation of the two proposed focusing strategies in this study is that the target exhibits sharp edges when it is within the focal plane.

1. Introduction

Automated focusing technology under the microscope has important significance in micro-operation, micro-assembly and scientific research. It can improve the accuracy, efficiency and reliability of experiments and has become one of the indispensable technical means in modern biotechnology and industrial production [1–3]. In micro-assembly, it is necessary to assemble some small and complex devices, which are very easy to be misoperated or damaged. Therefore, accurate operation can only be carried out under very clear images. Fast focusing technology can greatly improve the efficiency of micro-assembly, reduce the chance of misoperation, and also improve the accuracy and reliability of operation [4–6]. In micro-operation, micro-actuators usually need to perform single or multiple operations on cells, such as grabbing, releasing or injecting liquid into cells. In order to realize these operations, micro-actuators need to perform high-precision manipulation on cells at a specified depth [2,3,7–9]. Automatic focusing technology is the key to achieve target z-axis positioning. The less time consumed in focusing process, the higher the efficiency of micro-operation system. A fast and stable automatic focusing method can not only ensure the success rate of micro-operation system but also improve the efficiency of operation.

The automatic focusing method under the microscope can be divided into two categories: active focusing method based on distance measurement and passive focusing method based on image analysis. The active focusing based on distance measurement is achieved by adding additional distance sensors. For example, adding lasers [10,11], light-emitting diodes [12] or cameras [13] to measure the relative distance for focusing. This kind of active focusing method usually needs to modify the microscope optical path, so it is not suitable for general microscope operation systems.

Passive focusing based on image analysis relies on image analysis algorithms. Compared with active focusing, passive focusing does not require additional distance sensors, but determines the correct focus position by analyzing existing image information [14]. This method can usually be directly adapted to existing microscope systems and has relatively lower cost, so it is more popular. Passive focusing can be mainly divided into three categories: (1) automatic focusing based on phase detection [15]; (2) depth from defocus [4,8,16–20]; (3) depth from focus [21–23].

Automatic focusing based on phase detection: Phase detection method can determine the defocus distance and defocus direction of

[☆] This document is the results of the research project funded by the Innovative Institute of Basic Medical Sciences of Zhejiang University.

* Corresponding author.

E-mail address: huiquanwangzju@163.com (H. Wang).

the object. In the microscope, this kind of automatic focusing detection method is only suitable for a small amount of wide-field microscopes. These wide-field microscopes have main and secondary cameras. When the object is out of focus, the images of the main and secondary cameras will appear lateral displacement [15]. The defocus distance of the object can be characterized by the displacement amount, thus realizing defocus distance detection.

Depth-from-Defocus (DFD): Automatic focusing technology based on Depth-from-Defocus (DFD) extracts parameters that characterize the distance between the object and the focal plane through image processing to estimate the defocus distance of the object. DFD method requires capturing two or more images for analyzing defocus distance [19]. Ordinary imaging cameras estimate defocus distance by changing internal camera parameters to obtain different images [14]. However, it is not feasible to achieve automatic focusing by changing internal camera parameters settings because microscope optical path properties cannot be modified. The existing DFD method used for microscopes requires prior knowledge of clear images of the focused object. The current image is compared with the clear image to estimate defocus parameters [4,17]. Another DFD method used for microscopes extracts defocus information through deep learning methods, which has low universality and is only applicable to specific targets [8,20].

Depth-from-focus: Depth-from-focus determines whether focusing is completed by analyzing the sharpness of the image. Focusing is considered to be completed when the maximum value of image sharpness is reached. The focusing method based on sharpness is usually subject to some limitations and defects, mainly including the following points: (1) The trade-off between sharpness discrimination accuracy and noise resistance. Algorithms with high sharpness discrimination accuracy are more sensitive to identifying gradient changes but may be more susceptible to noise interference, resulting in misjudgment. Conversely, algorithms with strong noise resistance may ignore some small sharpness changes, affecting the accuracy of focusing [3,9]. (2) Lack of a clear focusing threshold. The sharpness of an image is affected by many factors such as image resolution and light intensity. This implies that there is no unified threshold to determine whether an object is near the focal plane, and repeated motion is needed to find the optimal focusing position [24].

This article proposes an improved filtering operator based on the first-order derivative Gaussian filtering operator (IGO) which can roughly realizes point spread function (PSF) parameter estimation in single-image and two new focusing strategies combined with PSF parameter estimation method to achieve fast and stable focusing. This method belongs to passive focusing method and is suitable for ordinary imaging microscopes. The structure of this article is arranged as follows: Section 2 mainly describes the derivation process of the IGO from the PSF model, Section 3 mainly describes the focusing strategy, and Section 4 describes the experimental verification of PSF parameter estimation and the experimental verification of focusing strategy.

2. PSF parameter estimation

2.1. PSF model

The point spread function (PSF) of the imaging system describes how the system spreads an ideal light point (called a point source) into a finite-sized spot on the image sensor. If the imaging system is defocused, the point source will spread over multiple pixels [17,25].

In incoherent imaging systems, the image of an object can be regarded as the convolution of the true object and PSF. If the real image is denoted as $f(x, y)$, the two-dimensional Gaussian filtering is $h(x, y)$:

$$h(x, y) = \frac{1}{2\pi\sigma^2} e^{-\frac{x^2+y^2}{2\sigma^2}} \quad (1)$$

So, the real imaging of the microscope is:

$$g(x, y) = \frac{1}{2\pi\sigma^2} \iint f(u, v) e^{-\frac{(x-u)^2+(y-v)^2}{2\sigma^2}} dudv \quad (2)$$

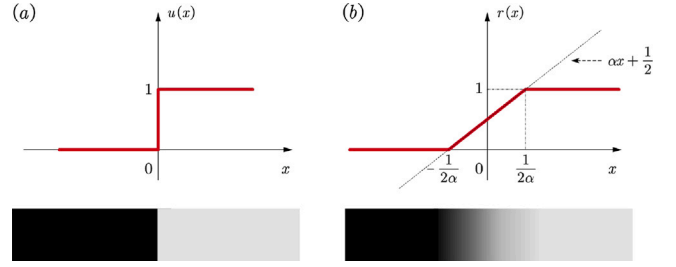


Fig. 1. (a) The schematic illustration of function $u(x)$. (b) The schematic illustration of function $r(x)$. At the bottom is the corresponding one-dimensional edge schematic.

$$\sigma = \frac{\epsilon \cdot f \cdot D}{k(u_0 + \epsilon)(u_0 - f)} \quad (3)$$

where, σ is the point spread parameter, ϵ is the defocus distance, k is the ratio of the previous two parameters, u_0 is the distance between the object and the objective lens when the image is clear, f is the focal length of the objective lens, and D is the diameter of the objective lens. The clearer the object is imaged, the smaller σ is.

2.2. Estimation method in one-dimension

We first consider the one-dimensional case. In the absence of noise, ideal image edges can be represented by step functions, and M represents amplitude:

$$f(x) = Mu(x) \quad (4)$$

$u(x)$ here is step function, as shown in Fig. 1(a).

One-dimensional Gaussian filtering is:

$$G(x) = \frac{1}{\sqrt{2\pi}\sigma_1} e^{-\frac{x^2}{2\sigma_1^2}} \quad (5)$$

The imaging of the edge when it is out of focus is:

$$F_1(x) = f(x) * G(x) = M \left(\frac{1}{2} + \frac{\text{erf}\left(\frac{x}{\sqrt{2}\sigma_1}\right)}{2} \right) \quad (6)$$

The first-order Gaussian filtering template is an edge extraction template, which is a high-pass filter. Its expression is as follows:

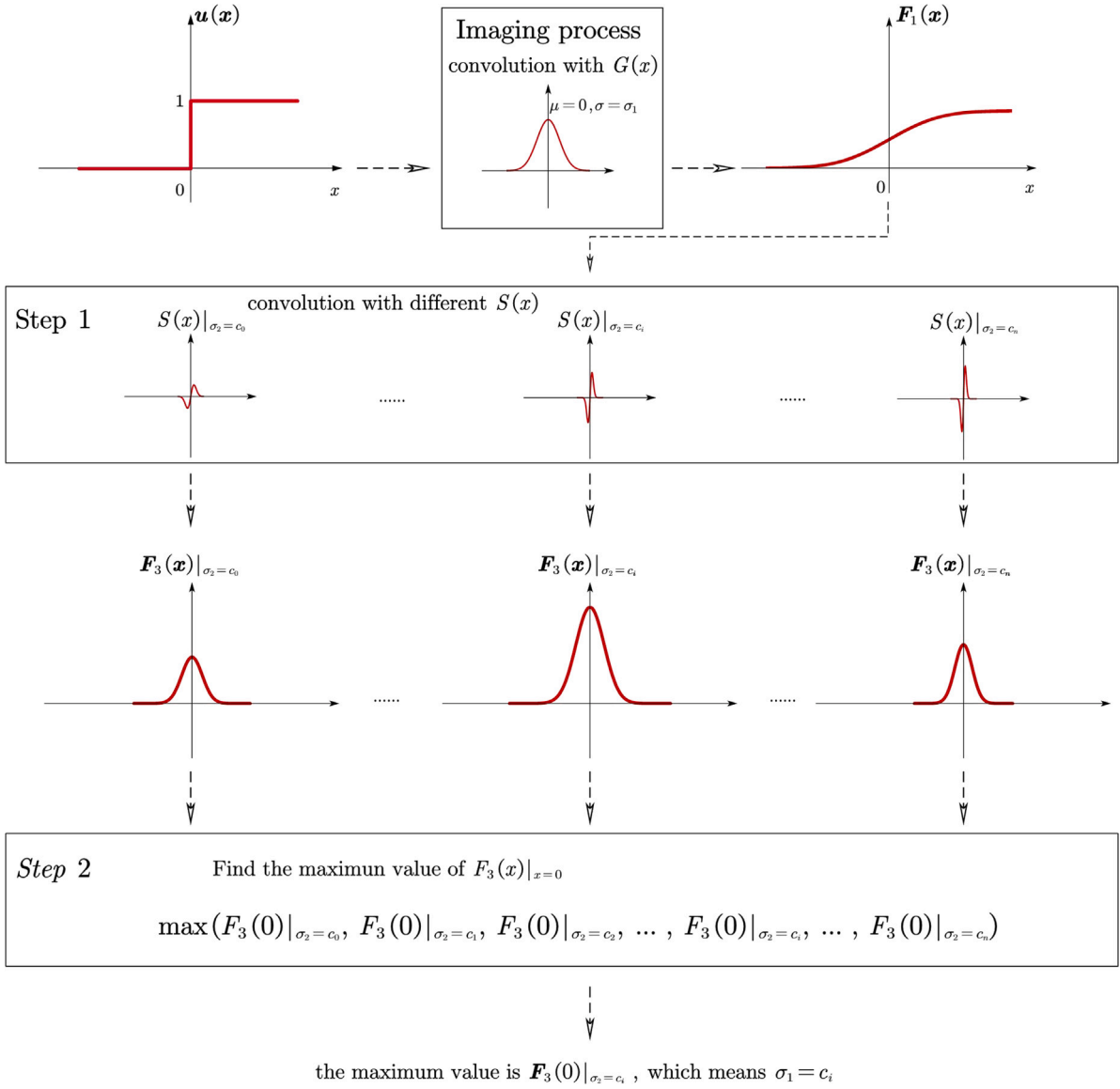
$$G'(x) = -\frac{1}{\sqrt{2\pi}\sigma_2^3} x e^{-\frac{x^2}{2\sigma_2^2}} \quad (7)$$

We consider the response of the edge point to the first-order Gaussian filter. Here, since the edge function is a step function, $x = 0$ is the edge point:

$$\begin{aligned} F_2(0) &= F_1(x) * G'(x)|_{x=0} \\ &= \left. \frac{M e^{-\frac{x^2}{2(\sigma_1^2+\sigma_2^2)}}}{\sqrt{2\pi}\sqrt{\sigma_1^2+\sigma_2^2}} \right|_{x=0} \\ &= \frac{M}{\sqrt{2\pi}\sqrt{\sigma_1^2+\sigma_2^2}} \end{aligned} \quad (8)$$

Multiplying both sides of Eq. (8) by $\sqrt{2\pi}\sigma_2$ yields:

$$F_3(0) = \sqrt{2\pi}\sigma_2 F_2(0) = \frac{M}{\sqrt{\frac{\sigma_1^2}{\sigma_2^2} + \sigma_2}} \quad (9)$$

Fig. 2. σ_1 estimation process.

From Eq. (9), it can be seen that the maximum value of $F_3(0)$ is obtained when $\sigma_2 = \sigma_1$. We can deduce by reversing the equation $F_3(x)$:

$$F_3(x) = \sqrt{2\pi\sigma_2} F_1(x) * G'(x) = F_1(x) * \left(\sqrt{2\pi\sigma_2} G'(x) \right) \quad (10)$$

Therefore, we can obtain a new filtering operator:

$$S(x) = \sqrt{2\pi\sigma_2} G'(x) = -\frac{1}{\sigma_2} x e^{-\frac{x^2}{2\sigma_2^2}} \quad (11)$$

When $\sigma_2 = \sigma_1$, the edge response of $S(x)$ is the most intense. Hence, we can adopt various $S(x)$ to perform convolution processing on image edges, achieving σ_1 estimation, as shown in Fig. 2. We call $S(x)$ the improved Gaussian first-order operator (IGO).

In the previous discussions, we considered the boundaries of abrupt mutations. However, in reality, there exist many edges characterized by smooth changes. In order to validate the universality of $S(x)$, we hypothesize the following function $r(x)$ to approximate edges with

gradual transitions.

$$r(x) = \begin{cases} 0, & x < -\frac{1}{2\alpha} \\ \alpha \left(x + \frac{1}{2\alpha} \right), & x < \frac{1}{2\alpha} \\ 1, & x \geq \frac{1}{2\alpha} \end{cases} \quad (12)$$

The schematic illustration of $r(x)$ is shown in Fig. 1(b). α in the Eq. (12) is a scaling factor. One can simulate the degree of variation in edge by manipulating the value of α . As $\alpha \rightarrow 0$, $r(x) \rightarrow 0$, and as $\alpha \rightarrow +\infty$, $r(x)$ approximates to $u(x)$. Hence, the one-dimensional edge $f_r(x)$ is:

$$f_r(x) = M r(x) \quad (13)$$

Because $r(x)$ could be seen as:

$$r(x) = \int \alpha \left[u \left(x + \frac{1}{2\alpha} \right) - u \left(x - \frac{1}{2\alpha} \right) \right] dx \quad (14)$$

the response of $f_r(x) * G(x)$ to $S(x)$ at $x = 0$ could be written as:

$$\begin{aligned}
 F_{3r}(0) &= \sqrt{2\pi\sigma_2} F_{2r}(0) \\
 &= \sqrt{2\pi\sigma_2} f_r(x) * G(x) * G'(x) \Big|_{x=0} \\
 &= f_r(x) * G(x) * S(x) \Big|_{x=0} \\
 &= \sqrt{2\pi\sigma_2} \int M\alpha \left[u\left(x + \frac{1}{2\alpha}\right) - u\left(x - \frac{1}{2\alpha}\right) \right] \\
 &\quad * G(x) * G'(x) dx \Big|_{x=0} \\
 &= \frac{M\alpha\sqrt{2\pi\sigma_2}}{2} \operatorname{erf}\left(\frac{1}{\sqrt{2\alpha}\sqrt{(\sigma_1^2 + \sigma_2^2)}} \right)
 \end{aligned} \tag{15}$$

For Eq. (15), we discuss it under three distinct cases: as α tends to infinity, as α takes on a constant value, and as α tends to infinitesimal values:

(1) α tends to infinity: in this case, $r(x)$ will become $u(x)$, and likely wise, $F_{3r}(0)$ will become $F_3(0)$:

$$F_{3r}(0) \Big|_{\alpha \rightarrow \infty} = \frac{M}{\sqrt{\frac{\sigma_1^2}{\sigma_2} + \sigma_2}} = F_3(0) \tag{16}$$

This represents an ideal case where $S(x)$ can accurately estimate σ_1 .

(2) α tends to infinitesimal values: in this case, which means the absence of edges, $r(x) = 0$, and $F_{3r}(0) = 0$.

(3) α takes on a constant value: Regarding the error function $\operatorname{erf}(\cdot)$, when the input is less than $\frac{1}{2}$, the output can be approximated as the input with an error within 5%. However, when the input exceeds $\frac{1}{2}$, the output gradually approaches 1. Hence, when $\frac{1}{\sqrt{2\alpha}\sqrt{(\sigma_1^2 + \sigma_2^2)}} < \frac{1}{2}$,

i.e., $\alpha\sqrt{(\sigma_1^2 + \sigma_2^2)} > \sqrt{2}$:

$$\begin{aligned}
 F_{3r}(0) &\sim \frac{M\alpha\sqrt{2\pi\sigma_2}}{2} \frac{1}{\sqrt{2\alpha}\sqrt{(\sigma_1^2 + \sigma_2^2)}} \\
 &= \frac{\sqrt{\pi}M}{2\sqrt{\frac{\sigma_1^2}{\sigma_2} + \sigma_2}}
 \end{aligned} \tag{17}$$

and in this case, one can still use $S(x)$ to get a reasonably accurate estimation of the value of σ_1 .

When $\frac{1}{\sqrt{2\alpha}\sqrt{(\sigma_1^2 + \sigma_2^2)}} > \frac{1}{2}$, i.e., $\alpha\sqrt{(\sigma_1^2 + \sigma_2^2)} < \sqrt{2}$,

$$F_{3r}(0) \sim \frac{M\alpha\sqrt{2\pi\sigma_2}}{2} \tag{18}$$

and in this case, one cannot use $S(x)$ to get a reasonably accurate estimation of the value of σ_1 . If $\alpha\sqrt{(\sigma_1^2 + \sigma_2^2)} > \sqrt{2}$, it can rigorously ensure $\alpha\sqrt{(\sigma_1^2 + \sigma_2^2)} > \sqrt{2}$. Thus, when the true value of σ_1 is greater than $\frac{\sqrt{2}}{\alpha}$, we can get a reasonably accurate estimation of the value of σ_1 . This implies that, for edges with gradual variations, i.e., the value of α is small, at larger defocus distances, $S(x)$ remains effective, however, at smaller defocus distances, $S(x)$ becomes ineffective; whereas for edges with prominent variations, i.e., the value of α is great, even when the defocus distance is small, $S(x)$ remains effective.

2.3. IGO operator in two-dimension

We extend the new filtering operator from one dimension to two dimensions. Here, we omit the derivation process (see Appendix A for the specific derivation process).

$$\begin{cases} S_x(x, y) = -\frac{x}{\sqrt{2\pi\sigma_2^2}} e^{-\frac{x^2+y^2}{2\sigma_2^2}} \\ S_y(x, y) = -\frac{y}{\sqrt{2\pi\sigma_2^2}} e^{-\frac{x^2+y^2}{2\sigma_2^2}} \end{cases} \tag{19}$$

It is easy to see from Eq. (19) that, like the two-dimensional Gaussian first-order operator, the new filtering operator is also a steerable operator [26]. The maximum response of this filter at a certain point can be calculated by the following method:

$$\begin{cases} F_x(x, y) = S_x(x, y) * f(x, y) \\ F_y(x, y) = S_y(x, y) * f(x, y) \end{cases} \tag{20}$$

$$F_{\max}(x, y) = \sqrt{(F_x(x, y))^2 + (F_y(x, y))^2} \tag{21}$$

Compared with the Gaussian first-order derivative filter, IGO only differs by a factor of $\sigma_2^{\frac{1}{2}}$, and from the perspective of frequency domain analysis, IGO is a band-pass filter like the Gaussian first-order derivative filter. Therefore, the response of the original image edge to IGO is much greater than that of non-edge points. Based on this characteristic, we use the total energy to approximate the energy of the response of IGO at the edge of the image.

$$E = \sum_i \sum_j [F_{\max}(i, j)]^2 \tag{22}$$

Based on Eq. (9), we can draw the following conclusion: the smaller the distance between σ_2 and σ_1 , the greater the value of E . In other words, we can use IGO with different values of σ_2 to convolve with the original image so that the value of σ_2 corresponding to the IGO operator with the maximum value of E is the value of σ_1 that we want to estimate, denoted as $\hat{\sigma}_1$.

Fig. 3 shows the value of E calculated by Eqs. (20)–(22). It can be observed that as the value of IGO parameter σ_2 increases, the value of E first increases and then decreases, showing a unimodal trend. When the image is more defocused, the value of $\hat{\sigma}_1$ is also larger. Calculating $\hat{\sigma}_1$ is a problem of locating extremum on a unimodal curve. Fast implementation schemes for such problems have been fully studied and will not be discussed in this paper.

3. Autofocus strategy

Ideally, if the image is not out-of-focus, then $\sigma_1 = 0$. Therefore, as the defocus distance decreases, σ_1 must tend to 0. Moreover, σ_1 is different from the image sharpness value. It is not affected by factors such as illumination, exposure time, and resolution. Based on this characteristic, we propose a focusing strategy that can achieve fast focusing without the microscope z-axis performing reciprocating motion.

In actual engineering implementation, automatic focusing strategies usually use the hill-climbing (HC) strategy and are divided into two steps: “coarse search” and “fine search”. As shown in Fig. 4(a) the coarse search uses a larger step size to push the focusing motor and searches for the peak value of the sharpness; the fine search switches to a smaller step size and searches until a more accurate peak position is found to achieve focusing. Compared with global search strategies, hill-climbing algorithms have the advantage of high speed, but they are susceptible to becoming trapped in local optimal points. This is especially true when the object is far away from the focal plane, as the evaluation function of image sharpness is highly vulnerable to noise, causing the hill-climbing algorithm to fail to achieve proper focus.

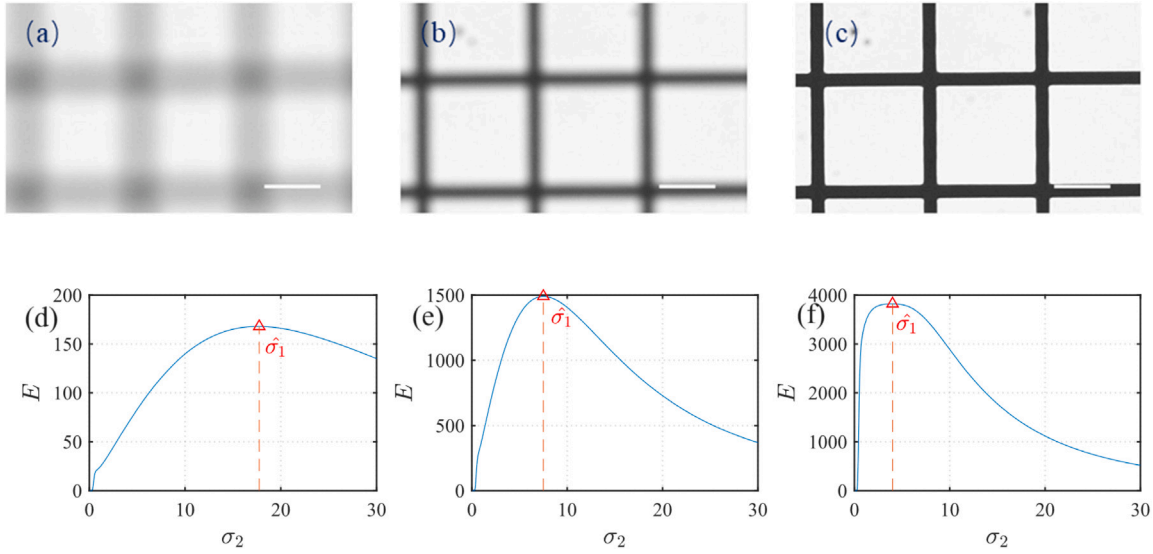


Fig. 3. $\hat{\sigma}_1$ estimation. (a) Very heavily defocused image. (b) Heavily defocused image. (c) Slightly defocused image. (d) $\hat{\sigma}_1$ estimation curve of image(a). (e) $\hat{\sigma}_1$ estimation curve of image(b). (f) $\hat{\sigma}_1$ estimation curve of image(c). The white line segment in the figure represents 50 μm . Observing figures (d)–(f) easily reveals that E represents a unimodal curve that changes with the value of σ_2 , and the value of σ_2 corresponding to the peak point is the final value of $\hat{\sigma}_1$. The smaller the defocus distance, the smaller the value of $\hat{\sigma}_1$.

To address the issue of the hill-climbing algorithm easily getting trapped in local optima while ensuring focusing speed, we propose two search strategies. We called the first strategy as IGO based search strategy (IGOSS), and the second strategy as IGO assisted hill-climbing search strategy (IGOAHC).

3.1. IGO based search strategy

Based on the previous analysis of the IGO operator, we can know that if most of the edges in the region of interest (ROI) are edges with prominent variations, regardless of whether the defocus distance is large or small, the IGO operator can accurately estimate the value of σ_1 . Therefore, for such a case, we propose the following focusing strategy.

As shown in Fig. 4(b), We use the coarse-to-fine search approach in IGOS. In the coarse search, we judge whether the object is near the focal plane by $\hat{\sigma}_1$. If the object is near the focal plane, we stop the coarse search and start the fine search. This strategy has the following advantages: (1) it avoids the problem of hill-climbing algorithm falling into local optima; (2) before the sharpness value crosses the peak value, we locate the watershed between “coarse search” and “fine search”, so as to achieve a transition from “coarse search” to “fine search” before crossing the peak value and improve focusing efficiency. The flow chart of IGOS is shown in Fig. 5, we set a constant a , when $\hat{\sigma}_1 > a$, we perform coarse search, when $\hat{\sigma}_1 < a$, we perform fine search with small step length. C_i represents the sharpness value of the current frame image and C_{i-1} represents the sharpness value of the last frame image.

3.2. IGO assisted hill-climbing search strategy

The IGOS system requires frequent convolutional calculations, and it may not be suitable for scenarios with insufficient computational power. In order to achieve fast and stable focusing in such situations, we need an alternative focusing strategy. The HC algorithm is prone to getting trapped in local optima when the object is far away from the focal plane, but it is less likely to occur when the defocus distance is small. The value of σ_1 can be accurately estimated by using IGO when the defocus distance is large, but not when the defocus distance is small. It is easy to observe that the effects of IGO and HC are complementary. Leveraging this characteristic, we only need to use IGO to determine whether HC’s judgment regarding focus completion is correct.

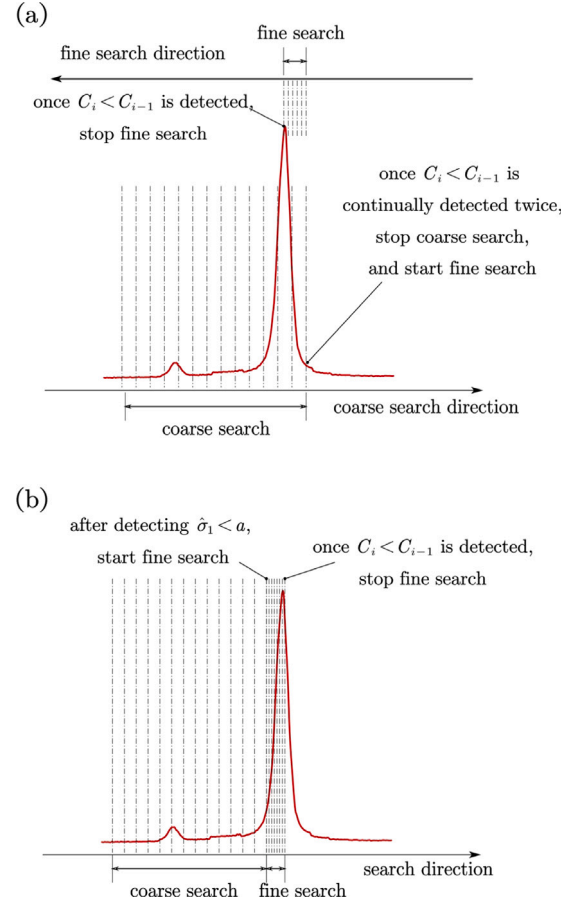


Fig. 4. The schematic diagram of the HC and IGOS, with the red curve representing the variation of sharpness. (a) The schematic diagram of HC. (b) The schematic diagram of IGOS.

We also use the coarse-to-fine search approach in IGOAHC. As shown in Fig. 6, in the coarse search, we calculate the contrast value C_i for the current image and compare it with the contrast value C_{i-1} from

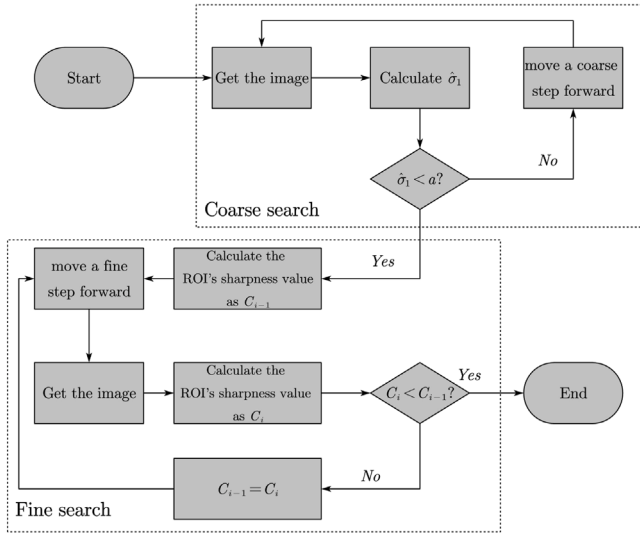


Fig. 5. Flow chart of IGOSS.

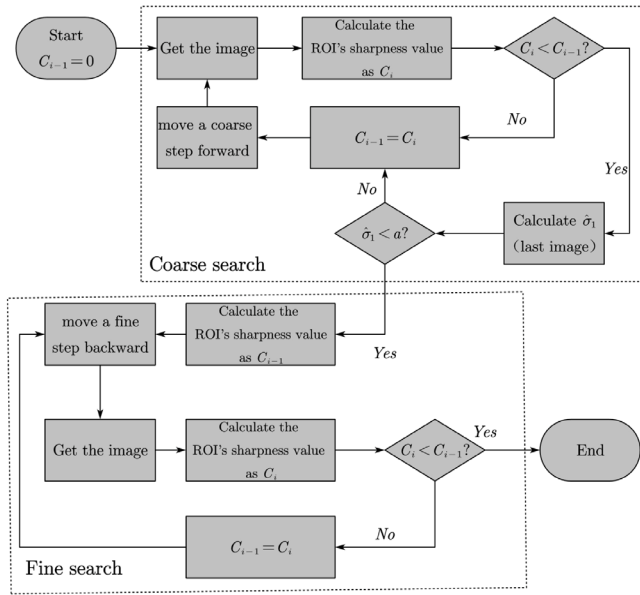


Fig. 6. Flow chart of IGOAHC.

the previous frame. If $C_i < C_{i-1}$, we begin to judge whether the value of σ_1 of last image is smaller than a . If $\hat{\sigma}_1 < a$, we alter the search direction and perform fine search; otherwise, we proceed with coarse search. This strategy avoids the problem of hill-climbing algorithm falling into local optima. In comparison to IGOSS, it exhibits greater universality but slightly lower efficiency due to the requirement of reverse movement.

3.3. Method for determining $\hat{\sigma}_1 < a$

Using the method in the “PSF Parameter Estimation” section, we can obtain $\hat{\sigma}_1$. However, as the true value of σ_1 increases, the calculation process of determining $\hat{\sigma}_1$ takes longer. This is because only the lower limit of σ_1 is known and the upper limit of σ_1 cannot be determined. If we directly use the method in the “PSF Estimation” section to obtain $\hat{\sigma}_1$, as the true value of σ_1 increases, we need to use a larger IGO convolution kernel to convolve the image, and the calculation amount will increase quadratically. This means that the coarse search process

cannot complete real-time analysis of the image. Therefore, a new method is needed to determine whether $\hat{\sigma}_1 < a$.

Firstly, two IGO operators are given, and their values are denoted as σ_{21} and σ_{22} respectively, and $\sigma_{21} < \sigma_{22}$. The energy value obtained by calculating with these two IGO operators are denoted as E_1 and E_2 , respectively. Combined with Eq. (9), it can be seen that:

$$\frac{E_1}{E_2} = \frac{\frac{\sigma_1^2}{\sigma_{22}} + \sigma_{22}}{\frac{\sigma_1^2}{\sigma_{21}} + \sigma_{21}} \quad (23)$$

By observing Eq. (23), we can find that:

$$\left. \frac{E_1}{E_2} \right|_{\sigma_1 \rightarrow +\infty} = \frac{\sigma_{21}}{\sigma_{22}} < 1 \quad (24)$$

$$\left. \frac{E_1}{E_2} \right|_{\sigma_1 \rightarrow 0} = \frac{\sigma_{22}}{\sigma_{21}} > 1 \quad (25)$$

$\sigma_1 \rightarrow +\infty$ represents the situation of severe image blurring, while $\sigma_1 \rightarrow 0$ represents the situation of no image blurring. It can be observed that in cases of severe image blur, $E_2 > E_1$, while in the absence of image blurring, $E_2 < E_1$. Furthermore, since both E_1 and E_2 monotonically increase with σ_1 , there must exist a constant c such that $E_2 < E_1$ for $\sigma_1 < c$ and $E_2 > E_1$ for $\sigma_1 > c$. The value of c is determined by σ_{21} and σ_{22} :

When $\sigma_1 = c$ and $\frac{E_1}{E_2} = 1$, then

$$\sigma_{21}\sigma_{22} = c^2 \quad (26)$$

Based on the above derivation, we can select two IGO operators and adjust σ_{21} and σ_{22} to make $c = a$, i.e., $\sigma_{21}\sigma_{22} = a^2$. Then, by determining whether $E_2 < E_1$, we can determine whether $\hat{\sigma}_1 < a$. This will effectively reduce the computational complexity during coarse search process.

4. Result

In our experimental verification platform, the microscope model is Olympus IX83 and the camera model is Olympus DP74.

4.1. σ_1 Estimation

In order to verify the capability of the IGO operator, we conducted σ_1 estimation tests on various samples, namely grid ruler, micro-pipette, woody dicot stem, epidermis under corn leaves, and intestine slice. The ROI region as shown in Fig. 7. These samples can be regarded as representing the following scenarios: (a) Grid rulers: an ideal case where only abrupt edges exist; (b) Micro-pipette: a situation where smooth edges coexist with abrupt edges; (c) Woody dicot stem and Epidermis under corn leaves: dominant presence of abrupt edges; (d) Intestine: Scenario with no significant edges.

We considered the image with the maximum sharpness value as the fully focused image and performed σ_1 estimation on the preceding and succeeding 50 images. The sampling interval for each frame image was set at 2 μm . As shown in the figure below, Fig. 8(a) shows the σ_1 estimation results under 10 \times objective lens, Fig. 8(b) shows the σ_1 estimation results under 20 \times objective lens, Fig. 8(c) shows the σ_1 estimation results under 40 \times objective lens.

From the experimental results, it can be seen that the smaller the defocusing distance, the smaller the value of $\hat{\sigma}_1$, and $\hat{\sigma}_1$ tends to approach 0, which is consistent with the theoretical derivation. However, different samples yield varying $\hat{\sigma}_1$ values at the same defocus distance, indicating that this method cannot accurately estimate the defocus distance. Nonetheless, this does not hinder our focusing strategy, as there still exists a trend that σ_1 towards 0 as the defocus distance decreases. It is easy to find from the change curve of $\hat{\sigma}_1$ that when the defocusing distance is near to 0, its value no longer decreases. The reason is detailed in Appendix B. This is also the reason why we do not directly use $\hat{\sigma}_1$ to determine whether the microscope has completed focus both in IGOSS and IGOAHC.

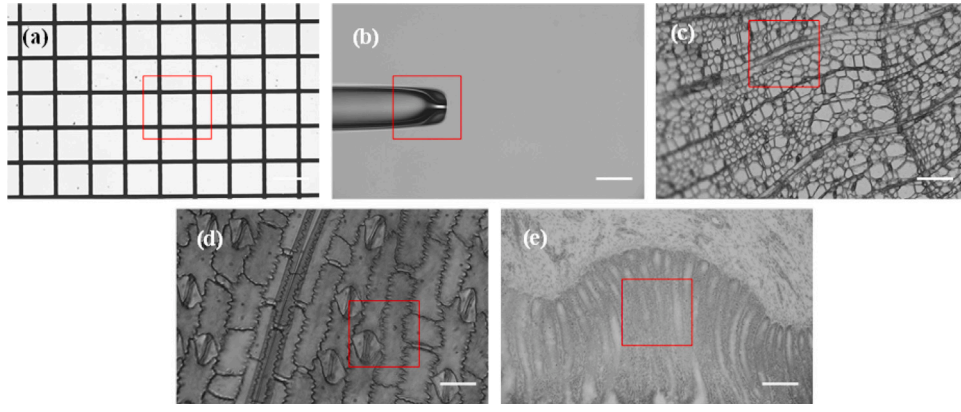


Fig. 7. The ROI region (The white line segment in the figure represents 100 μm , and all the images captured by 20 \times objective lens). (a) Grid ruler. (b) Micro-pipette. (c) Woody dicot stem. (d) Epidermis under corn leaves. (e) Intestine.

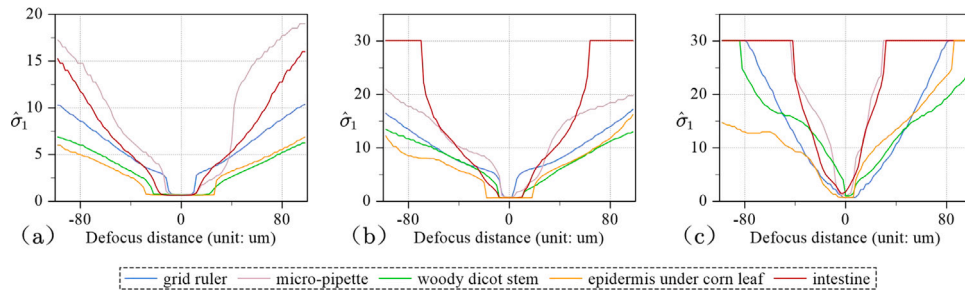


Fig. 8. $\hat{\sigma}_1$ estimation result of different samples. (a) σ_1 estimation results under 10 \times objective lens. (b) σ_1 estimation results under 20 \times objective lens. (c) σ_1 estimation results under 40 \times objective lens. In experiments, we set the upper limit of $\hat{\sigma}_1$ to 30.

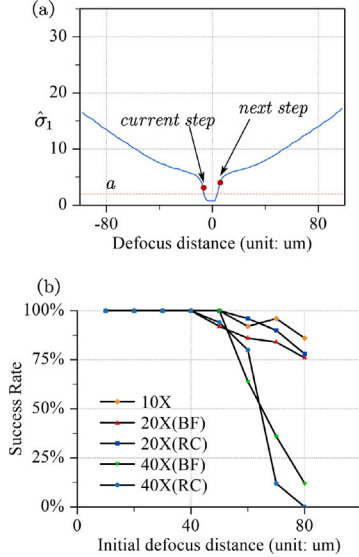


Fig. 9. (a) The case where $\hat{\sigma}_1 < a$ will not be detected if the coarse step size is great or the value of a is too small. (b) The success rate of HC only through fine search. BF represents the Bright Field imaging mode, and RC stands for the Robert Hoffman Modulation Contrast imaging mode.

4.2. Determine of coarse step size and the value of a

The size of coarse step and the value of parameter a have a significant impact on IGOSS and IGOAHC. If the value of parameter a is too large, both IGOSS and IGOAHC will degrade into the HC algorithm. On the other hand, if the value of parameter a is too small, a situation similar to Fig. 9(a) will occur, where in the previous frame, $\hat{\sigma}_1 > a$, and

in the subsequent frame, $\hat{\sigma}_1 > a$ again, directly skipping the case where $\hat{\sigma}_1 < a$. Similarly, if the size of the coarse step is too large, a situation as shown in Fig. 9(a) will also arise. Conversely, if the size of the coarse step is too small, it will prolong the focusing time.

Initially, we conducted autofocus experiments using the HC algorithm, and the grid ruler was used as the sample for the autofocus experiment. In this experiment, we only employed the fine step, where each step had a size of 2 μm . The success rate of autofocus was statistically analyzed for different initial positions, as shown in Fig. 9(b). According to the experimental results, it can be concluded that the HC algorithm demonstrates excellent robustness when the defocus distance is less than 40 μm . Therefore, we can set the value of $\hat{\sigma}_1$ obtained under the condition of a defocus distance equal to 40 μm as the critical threshold for the coarse search and fine search. Considering that the coarse search is much more efficient than the fine search, the $\hat{\sigma}_1$ obtained at a defocus distance of 20 μm is chosen as the critical threshold. By doing so, the overall time required for the entire autofocus process can be reduced. Therefore, after analyzing the $\hat{\sigma}_1$ estimation curves of the grid ruler at 10 \times , 20 \times , and 40 \times magnifications, we obtained the values of a to be 3, 7, and 7, respectively. The coarse step size is half of the 20 μm , which is 10 μm .

4.3. Autofocus

Autofocus verification was carried out using hill-climbing algorithm, curve fitting assisted autofocus algorithm (FAF) [27], Rule-based autofocus algorithm (RBAF) [24], and the algorithm proposed in this paper. The evaluation function for sharpness utilizes Energy of Gradient (EOG), which is also called Squared Gradient [28]. At 10 \times , 20 \times and 40 \times magnification. The curve fitting method used in FAF adopts the approach described in [29]. For HC, FAF, IGOSS and IGOAHC, the moving step size of coarse search is 10 $\mu\text{m}/\text{step}$, and that of fine search is 2 $\mu\text{m}/\text{step}$. For RBAF, the coarse step size is 30 $\mu\text{m}/\text{step}$, middle

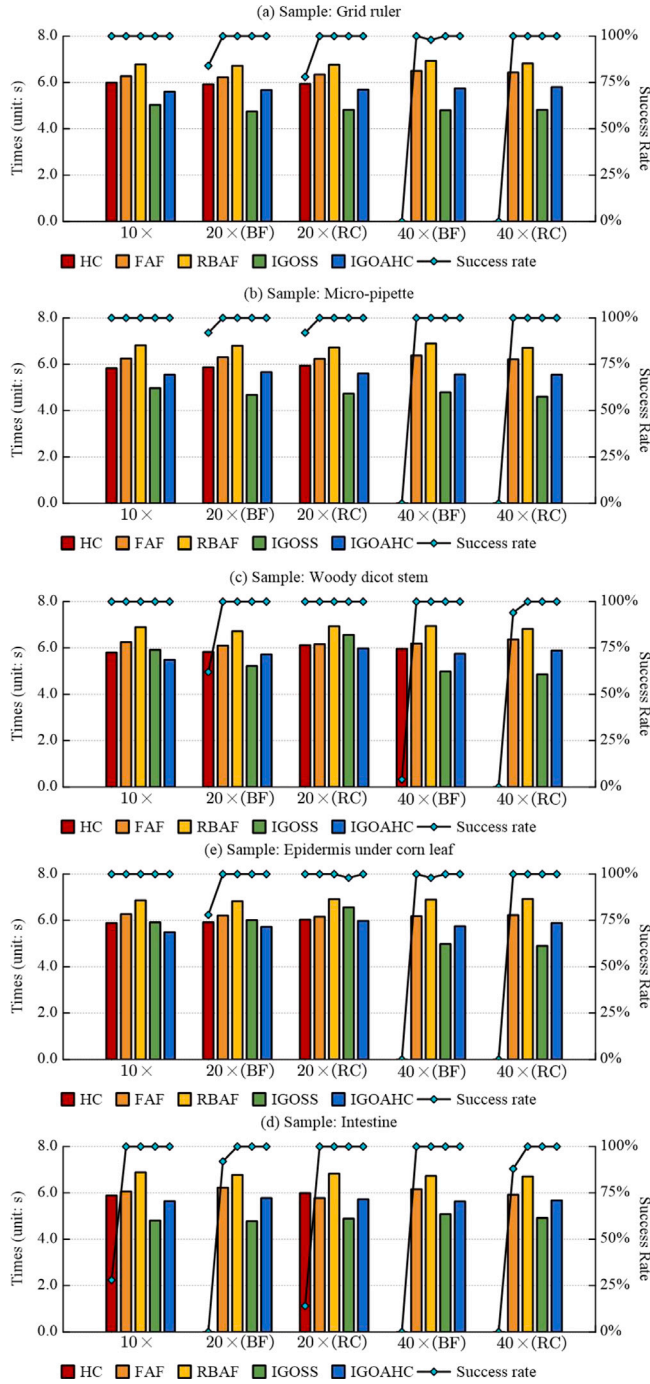


Fig. 10. Results of focus verification. (a) Test results using grid ruler as samples. (b) Test results using micro-pipette as samples. (c) Test results using woody dicot stem as samples. (d) Test results using intestine as samples. (e) Test results using epidermis under corn leaf as samples.

step size is 10 $\mu\text{m}/\text{step}$ and the fine step size is 2 $\mu\text{m}/\text{step}$. The initial position of the focusing axis is 200 μm away from the focus. When the focusing is completed, if the z -axis coordinate of the focusing axis is within the depth of field range when the image is clearest, it is considered as successful focusing. Each group was tested 50 times. The experimental results are shown in Fig. 10. (If focusing fails, the focusing time is not counted.)

Observing the experimental results, it can be found that: Compared to the HC algorithm, FAF, RBAF, IGOSS, and IGOAHC algorithms exhibit significantly improved robustness, with IGOAHC being

the most stable. The execution time of IGOSS and IGOAHC algorithms is generally lower than that of FAF and RBAF algorithms.

The stability of FAF is exceptionally high; however, it performs poorly in intestine samples due to the presence of bimodal sharpness value curves in certain regions of interest. If the peak with a lower sharpness value appears first, FAF converges to that local optimum point.

RBAF exhibits high stability, however, RBAF is the most time-consuming method among all the algorithms.

IGOSS algorithm demonstrates good stability; however, it exhibits significant fluctuations in autofocus execution time. In the case of woody dicot stem and epidermis under corn leaf test samples, IGOSS algorithm can approach the execution time of RBAF in certain scenarios. The reason for the time fluctuations in IGOSS can be found in Fig. 8(a)(b). Taking woody dicot stem as an example, under 10 \times magnification, $\hat{\sigma}_1 < a$ appears prematurely, leading to an increase in the number of steps in the fine search, consequently resulting in an increase in the autofocus time.

IGOAHC is an efficient autofocus algorithm that performs exceptionally well, especially in highmagnification situations. In these scenarios, the success rate of IGOAHC is remarkably high. Generally, the autofocus efficiency of IGOAHC may be lower than that of IGOSS, as IGOSS locates the watershed between “coarse search” and “fine search” before the sharpness value crosses the peak value. However, unlike IGOSS, the autofocus efficiency of IGOAHC is almost unaffected by samples. This means that IGOAHC can provide reliable autofocus service in both fast-focusing scenarios and situations demanding quick focusing time.

4.4. Time consumption testing of IGO operator

The gradient operator used for sharpness evaluation typically has a constant size of 3×3 . However, the size of the IGO operator varies depending on the value of σ_2 . Generally, the size of the IGO operator is determined as $6 \text{ ceil}(\sigma_2) \times 6 \text{ ceil}(\sigma_2)$. Therefore, the minimum size of the IGO operator is 6×6 . When σ_2 has a large value, the size of the IGO operator becomes significantly larger, resulting in a considerable increase in computational complexity. Hence, assessing the time consumption of the IGO operator is crucial. Fortunately, IGO is a separable convolution operator [30], which means that its computational complexity increases linearly with σ_2 .

We inputted ROI of sizes $200 \times 200, 300 \times 300, \dots, 1100 \times 1100$, and convolved them using IGO operators with σ_2 values of 2, 4, \dots , 20. The average time consumption was then recorded for each case, as shown in Fig. 11. The testing was conducted using the Eigen library in a C++ environment on a computer equipped with an Intel i7-9700 processor.

In the IGOSS and IGOAHC, when determining whether $\sigma_1 < a$, two calculations are required, resulting in a computation time that is 4–6 times longer than EOG. In order to reduce the time cost, parallel computing was employed in our experiments. In the experimental tests conducted in Section 4.3, we chose ROI sizes that were all smaller than 600×600 . Each calculation took an average of 8.92 ms longer compared to EOG. In the future experiments, we will introduce GPUs and employ heterogeneous computing techniques to further reduce computation time.

4.5. Limitation

Although IGOSS and IGOAHC perform well in the experimental objects in this study, we think that these methods are suitable for specialized scenarios, while general scenarios can only be used as auxiliary means. Observing the intestine sample in Fig. 8(c), as the defocus distance decreases, the value of $\hat{\sigma}_1$ shows a downward trend, but when it is in the focus plane, the value of $\hat{\sigma}_1$ is still relatively large (compared to other samples, the distance from 0 is larger). This is because the edge of the intestine sample is relatively smooth, and the true appearance of the sample in the focus plane is unknown, so

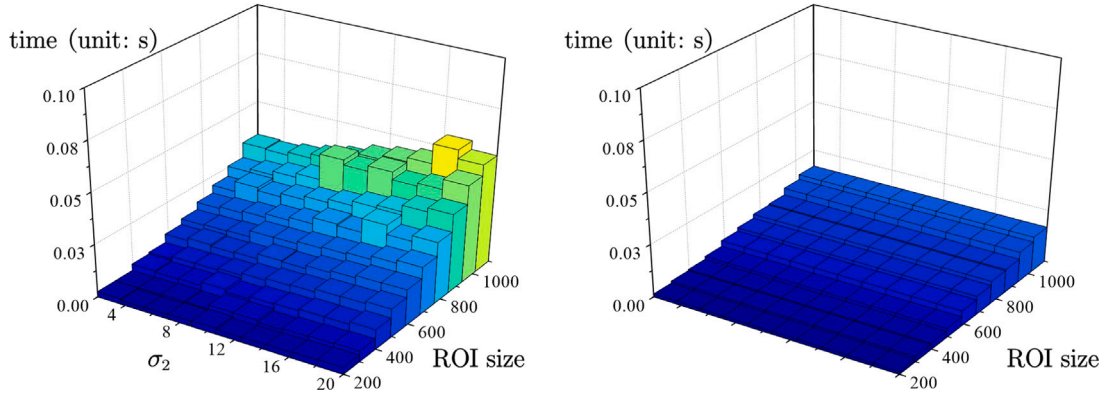


Fig. 11. Time consumption statistics. The left figure presents time consumption statistics for the IGO operator, while the right figure displays time consumption statistics for the EOG operator. A comparison of the two figures reveals that the time consumption of the IGO operator is approximately 2–3 times greater than that of the EOG operator.

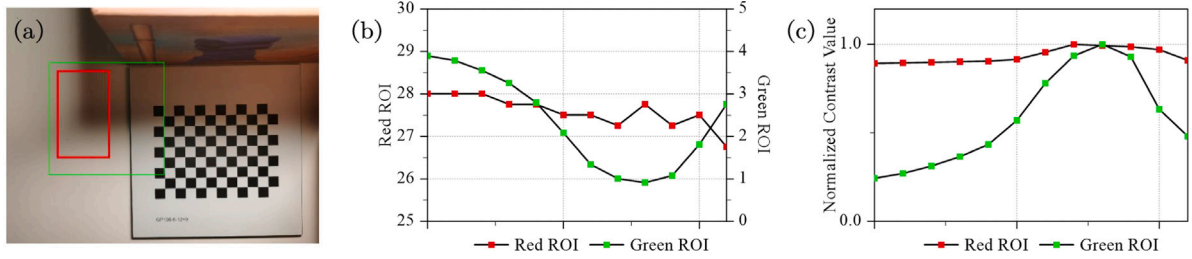


Fig. 12. The verification of IGO's limitation. (a) A macroscopic scenario with smooth edge. The red ROI contains the shadow of a box. The green ROI contains both the shadow and a chessboard pattern. (b) $\hat{\sigma}_1$ estimation result of these two ROIs. (c) The contrast value variation curve of these two ROIs.

IGO believes that the intestine sample is still in a defocused position when it is focused. Since we do not have real smooth edge samples, the experiments in this study do not demonstrate the limitations of this method. However, it is clear that this problem exists, and Eqs. (15) to (18) also demonstrate this limitation.

We constructed a macroscopic scenario and captured a series of images using a mobile phone to illustrate this issue. Fig. 12(a) demonstrates a clear image of this macroscopic scenario within the focal plane. The red ROI contains the shadow of a box, clearly showing its smooth edges. The green ROI contains both the shadow and a chessboard pattern, encompassing both smooth and sharp edges simultaneously. Fig. 12(b) presents the value of $\hat{\sigma}_1$ obtained through IGO. It can be observed that the $\hat{\sigma}_1$ estimates based on the red ROI consistently exhibit very high values, while those based on the green ROI display a trend towards 0. Therefore, if we choose the red ROI as the reference region, IGOSS and IGOAHC will never succeed. However, based on the curve of contrast values, as illustrated in Fig. 12(c), successful focusing can be accomplished.

Based on the aforementioned validation, we think that IGOSS and IGOAHC are more applicable in professional microscopy operation scenarios, such as cell micro-operation, microassembly, etc.. In automated cell micro-operation, the model of the micro-needle and the type of cells being manipulated are often specific. If we measure the curve of $\hat{\sigma}_1$ for a cell as a function of the defocus distance, we can consider this curve as the $\hat{\sigma}_1$ curve for other cells of the same type. The value of a determined based on this curve can also be generalized. Once the value of a is determined, we can design IGOSS and IGOAHC specifically for this type of cell. This ensures that the autofocus process is efficient and stable during automated micro-operations for this type of cell. Following the same method, IGOSS and IGOAHC for chips of Micro-Electro Mechanical System can also be designed in automated microassembly, achieving efficient and stable focusing. For batch production in the microassembly process, this can reduce production time.

In general scenarios, the combination of IGOSS or IGOAHC with RBAF can be employed. Taking the experiment in Section 4.3 as an

example, the coarse-step size of IGOAHC is 10 $\mu\text{m}/\text{step}$, whereas the coarse-step size of RBAF is 30 $\mu\text{m}/\text{step}$. Consequently, we can consider the three coarse-steps of IGOAHC as equivalent to one coarse-step of RBAF. If IGOSS or IGOAHC can achieve focusing, it will reduce the execution time of the focusing process. If IGOSS and IGOAHC cannot achieve focusing, RBAF can still ensure accurate focusing, but the execution time of the focusing process will increase.

In the future work, we will attempt to build a neural network for autofocus using different IGO and different gradient operators as convolutional templates to achieve a more generalized, highly reliable, and stable algorithm for autofocus.

5. Conclusion

In this paper, we introduced an improved filtering operator based on the first-order derivative Gaussian filtering operator. As the defocus distance decreases, the edges of an image transition from being smooth to sharp. Using the operator proposed in this study, a parameter can be obtained to quantify the degree of edge sharpness, where a smaller value indicates sharper edges. Taking advantage of this characteristic, we propose two novel focusing strategies: IGOSS and IGOAHC, which can effectively avoid the problem of HC algorithm converging at local optimal points. IGOSS can locate the watershed between “coarse search” and “fine search” before the clarity value crosses the peak value and achieve fast focusing. This is different from previous passive focusing strategies. However, the time consumption of IGOSS is susceptible to the influence of the samples. The efficiency of IGOAHC is comparable to that of HC, and it exhibits high stability. Although IGOSS and IGOAHC exhibit excellent performance, they require the size of the ROI to not be too large, as it can significantly increase the computational burden. Besides, the prerequisite for the successful implementation of the two proposed focusing strategies in this study is that the target exhibits sharp edges when it is within the focal plane. In the future work, we will introduce GPUs and employ heterogeneous computing techniques to further reduce computation time and attempt to build a

neural network for autofocus using different IGO and different gradient operators as convolutional templates to achieve a more generalized, highly reliable, and stable algorithm for autofocus.

Declaration of competing interest

The authors declare that they have no known competing financial interests or personal relationships that could have appeared to influence the work reported in this paper.

Data availability

Data will be made available on request.

Appendix A. Two-dimension IGO

Assuming a two-dimensional edge is an ideal edge perpendicular to the x -axis direction:

$$f(x, y) = u(x)y(1) \quad (27)$$

$u(\cdot)$ represents a step function and $y(1)$ represents a constant of 1 in the y -direction. The image obtained by the imaging system is:

$$F_1(x, y) = h(x, y) * f(x, y) = \frac{1}{2} + \frac{1}{2} \operatorname{erf}\left(\frac{x}{\sqrt{2}\sigma_1}\right) \quad (28)$$

The first-order derivative filtering of the two-dimensional Gaussian is:

$$h'_x(x, y) = -\frac{1}{2\pi\sigma_1^4} x e^{-\frac{x^2+y^2}{2\sigma_1^2}} \quad (29)$$

We did not consider the first-order derivative of the two-dimensional Gaussian in the y -direction here, as the edges are perpendicular to the x -direction. Therefore, the final response of the image to the first-order derivative filtering of the two-dimensional Gaussian in the y -direction is zero.

The response of the image to the first-order derivative filtering of the Gaussian is:

$$F_2(x, y) = F_1(x, y) * h'_x(x, y) = \frac{1}{\sqrt{2\pi}} e^{-\frac{x^2}{2(\sigma_1^2+\sigma_2^2)}} \quad (30)$$

Therefore, the response of the edges is:

$$F_2(0, y) = \frac{1}{\sqrt{2\pi}} \frac{1}{\sqrt{\sigma_1^2 + \sigma_2^2}} \quad (31)$$

The results are consistent with Eq. (8). Therefore, the expression of the IGO is as follows:

$$S_x(x, y) = \sqrt{2\pi}\sigma_2 h'_x(x, y) = -\frac{1}{\sqrt{2\pi}\sigma_2^{\frac{7}{2}}} x e^{-\frac{x^2+y^2}{2\sigma_2^2}} \quad (32)$$

Because IGO is a steerable control filter [26], we can directly provide an IGO operator suitable for any direction:

$$\begin{cases} S_x(x, y) = -\frac{x}{\sqrt{2\pi}\sigma_2^{\frac{7}{2}}} e^{-\frac{x^2+y^2}{2\sigma_2^2}} \\ S_y(x, y) = -\frac{y}{\sqrt{2\pi}\sigma_2^{\frac{7}{2}}} e^{-\frac{x^2+y^2}{2\sigma_2^2}} \end{cases} \quad (33)$$

Appendix B. The minimum effective value for σ_1 estimation

The Fourier transform expression of the continuous first-order derivative of the Gaussian is:

$$G'(j\omega) = j\omega\sqrt{2\sigma^2\pi}e^{-\frac{\sigma^2\omega^2}{2}} = j\omega\sqrt{2\sigma^2\pi}e^{-\frac{1}{2}\left(\frac{\omega}{\sigma}\right)^2} \quad (34)$$

The cutoff frequency of the Fourier expression can be approximated as:

$$\omega_s = \frac{3}{\sigma} \quad (35)$$

The sampling interval of the operator template is 1. If we want the discrete first-order Gaussian derivative template to effectively represent the continuous first-order Gaussian derivative template, then we have:

$$\frac{2\pi}{T} = 2\pi > 2\omega_s \quad (36)$$

Therefore, when $\sigma < \frac{3}{\pi}$, the discrete Gaussian first-order derivative template is distorted. Furthermore, it can be inferred that the discrete IGO is distorted when $\sigma_2 < \frac{3}{\pi}$. Therefore, when the true value of σ_1 is smaller than $\frac{3}{\pi}$, it cannot be accurately estimated.

References

- [1] X. Sha, W. Li, X. Lv, J. Lv, Z. Li, Research on auto-focusing technology for micro vision system, *Optik* 142 (2017) 226–233, <http://dx.doi.org/10.1016/j.ijleo.2017.06.001>, URL: <https://www.sciencedirect.com/science/article/pii/S0030402617306605>.
- [2] F. Sadak, M. Saadat, A.M. Hajiyavand, Three dimensional auto-alignment of the ICSI pipette, *IEEE Access* 7 (2019) 99360–99370, <http://dx.doi.org/10.1109/ACCESS.2019.2925465>.
- [3] W. Hu, H. Liang, J. Li, Z. Zhan, Y. Zhang, C. Hu, Three-dimensional positioning of the micropipette for intracytoplasmic sperm injection, in: 2021 IEEE International Conference on Robotics and Automation (ICRA), 2021, pp. 1249–1255, <http://dx.doi.org/10.1109/ICRA48506.2021.9561549>.
- [4] L. Chen, Z. Yang, L. Sun, Fast autofocus of microscopy images based on depth-from-defocus, in: 2008 IEEE/RSJ International Conference on Intelligent Robots and Systems, 2008, pp. 3115–3120, <http://dx.doi.org/10.1109/IROS.2008.4650658>.
- [5] F.D. Li, D. Xu, Z.T. Zhang, Y.L. Shi, Realization of an automated microassembly task involving micro adhesive bonding, *Int. J. Autom. Comput.* 10 (6) (2013) 7.
- [6] L. Chen, Z. Yang, L. Sun, Three-dimensional tracking at micro-scale using a single optical microscope, in: C. Xiong, H. Liu, Y. Huang, Y. Xiong (Eds.), *Intelligent Robotics and Applications*, Springer Berlin Heidelberg, Berlin, Heidelberg, 2008, pp. 178–187.
- [7] Z. Wang, C. Feng, W.T. Ang, S.Y.M. Tan, W.T. Latt, Autofocusing and polar body detection in automated cell manipulation, *IEEE Trans. Biomed. Eng.* 64 (5) (2017) 1099–1105, <http://dx.doi.org/10.1109/TBME.2016.2590995>.
- [8] Z. Wang, H. Gong, K. Li, B. Yang, Y. Du, Y. Liu, X. Zhao, M. Sun, Simultaneous depth estimation and localization for cell manipulation based on deep learning, in: 2022 IEEE/RSJ International Conference on Intelligent Robots and Systems (IROS), 2022, pp. 10432–10438, <http://dx.doi.org/10.1109/IROS47612.2022.9982228>.
- [9] L. Su, H. Zhang, H. Wei, Z. Zhang, Y. Yu, G. Si, X. Zhang, Macro-to-micro positioning and auto focusing for fully automated single cell microinjection, *Microsyst. Technol.* 27 (1) (2021) 11–21, <http://dx.doi.org/10.1007/s00542-020-04891-w>.
- [10] C.-S. Liu, P.-H. Hu, Y.-H. Wang, S.-S. Ke, Y.-C. Lin, Y.-H. Chang, J.-B. Horng, Novel fast laser-based auto-focusing microscope, in: *SENSORS*, 2010 IEEE, 2010, pp. 481–485, <http://dx.doi.org/10.1109/ICSENS.2010.5690153>.
- [11] J. Lightley, F. Görlitz, S. Kumar, R. Kalita, A. Kolbeinsson, E. Garcia, Y. Alexandrov, V. Bousgouni, R. Wysoczanski, P. Barnes, L. Donnelly, C. Bakal, C. Dunsby, M.A. Neil, S. Flaxman, P.M. French, Robust deep learning optical autofocus system applied to automated multiwell plate single molecule localization microscopy, *J. Microsc.* 288 (2) (2022) 130–141, <http://dx.doi.org/10.1111/jmi.13020>, URL: <https://onlinelibrary.wiley.com/doi/abs/10.1111/jmi.13020>, arXiv: <https://onlinelibrary.wiley.com/doi/pdf/10.1111/jmi.13020>.
- [12] J. Liao, Y. Jiang, Z. Bian, B. Mahrou, A. Nambiar, A.W. Magsam, K. Guo, S. Wang, Y. Ku Cho, G. Zheng, Rapid focus map surveying for whole slide imaging with continuous sample motion, *Opt. Lett.* 42 (17) (2017) 3379–3382, <http://dx.doi.org/10.1364/OL.42.003379>, URL: <https://opg.optica.org/ol/abstract.cfm?URI=ol-42-17-3379>.

- [13] K. Guo, J. Liao, Z. Bian, X. Heng, G. Zheng, InstantScope: a low-cost whole slide imaging system with instant focal plane detection, *Biomed. Opt. Express* 6 (9) (2015) 3210–3216, <http://dx.doi.org/10.1364/BOE.6.003210>, URL: <https://opg.optica.org/boe/abstract.cfm?URI=boe-6-9-3210>.
- [14] Y. Xiong, S. Shafer, Depth from focusing and defocusing, in: *Proceedings of IEEE Conference on Computer Vision and Pattern Recognition*, 1993, pp. 68–73, <http://dx.doi.org/10.1109/CVPR.1993.340977>.
- [15] L. Silvestri, M.C. Müllenbroich, I. Costantini, A.P. Di Giovanna, G. Mazzamuto, A. Franceschini, D. Kutra, A. Kreshuk, C. Checcucci, L.O. Husein Zilullah Torezano, P. Frascioni, L. Sacconi, F. Pavone, Universal autofocus for quantitative volumetric microscopy of whole mouse brains, *Nature Methods* 18 (2021) <http://dx.doi.org/10.1038/s41592-021-01208-1>.
- [16] E. Alexander, L.A. Kabuli, O.S. Cossairt, L. Waller, Depth from defocus as a special case of the transport of intensity equation, in: *2021 IEEE International Conference on Computational Photography (ICCP)*, 2021, pp. 1–13, <http://dx.doi.org/10.1109/ICCP51581.2021.9466260>.
- [17] Z. Xin, S. Mingzhu, Y. Bin, L. Guizhang, L. Jingtai, H. Dagang, Extracting depth information from microscopic image of micro manipulator, in: *2004 IEEE International Conference on Robotics and Biomimetics*, 2004, pp. 629–633, <http://dx.doi.org/10.1109/ROBIO.2004.1521853>.
- [18] B. Gutiérrez-Medina, M. de Jesús Sánchez Miranda, Quantitative image restoration in bright field optical microscopy, *Biophys. J.* 113 (9) (2017) 1916–1919, <http://dx.doi.org/10.1016/j.bpj.2017.09.002>, URL: <https://www.sciencedirect.com/science/article/pii/S0006349517309840>.
- [19] K. Takemura, T. Yoshida, Depth from defocus technique based on cross reblurring, *IEICE Trans. Inf. Syst.* E102.D (2019) 2083–2092, <http://dx.doi.org/10.1587/transinf.2019PCP0004>.
- [20] Y. Xiang, Z. He, Q. Liu, J. Chen, Y. Liang, Autofocus of whole slide imaging based on convolution and recurrent neural networks, *Ultramicroscopy* 220 (2021) 113146, <http://dx.doi.org/10.1016/j.ultramic.2020.113146>, URL: <https://www.sciencedirect.com/science/article/pii/S030439912030293X>.
- [21] Y. Sun, S. Duthaler, B. Nelson, Autofocusing algorithm selection in computer microscopy, in: *2005 IEEE/RSJ International Conference on Intelligent Robots and Systems*, 2005, pp. 70–76, <http://dx.doi.org/10.1109/IROS.2005.1545017>.
- [22] H. Zhang, J. Yao, Automatic focusing method of microscopes based on image processing, *Math. Probl. Eng.* 2021 (2021) 1–9, <http://dx.doi.org/10.1155/2021/8243072>.
- [23] Y. Yao, B. Abidi, N. Doggaz, M. Abidi, Evaluation of sharpness measures and search algorithms for the auto-focusing of high-magnification images, in: Z. ur Rahman, S.E. Reichenbach, M.A. Neifeld (Eds.), *Visual Information Processing XV*, Vol. 6246, International Society for Optics and Photonics, SPIE, 2006, 62460G, <http://dx.doi.org/10.1117/12.664751>.
- [24] N. Kehtarnavaz, H.-J. Oh, Development and real-time implementation of a rule-based auto-focus algorithm, *Real-Time Imag.* 9 (3) (2003) 197–203, [http://dx.doi.org/10.1016/S1077-2014\(03\)00037-8](http://dx.doi.org/10.1016/S1077-2014(03)00037-8), URL: <https://www.sciencedirect.com/science/article/pii/S1077201403000378>.
- [25] S. Zhuo, T. Sim, Defocus map estimation from a single image, *Pattern Recognit.* 44 (9) (2011) 1852–1858, <http://dx.doi.org/10.1016/j.patcog.2011.03.009>, URL: <https://www.sciencedirect.com/science/article/pii/S003132031100094X>, computer Analysis of Images and Patterns.
- [26] W. Freeman, E. Adelson, The design and use of steerable filters, *IEEE Trans. Pattern Anal. Mach. Intell.* 13 (9) (1991) 891–906, <http://dx.doi.org/10.1109/34.93808>.
- [27] C.-M. Chen, C.-M. Hong, H.-C. Chuang, Efficient auto-focus algorithm utilizing discrete difference equation prediction model for digital still cameras, *IEEE Trans. Consum. Electron.* 52 (4) (2006) 1135–1143, <http://dx.doi.org/10.1109/TCE.2006.273125>.
- [28] Y. Sun, S. Duthaler, B. Nelson, Autofocusing algorithm selection in computer microscopy, in: *2005 IEEE/RSJ International Conference on Intelligent Robots and Systems*, 2005, pp. 70–76, <http://dx.doi.org/10.1109/IROS.2005.1545017>.
- [29] D.-C. Tsai, H.H. Chen, Focus profile modeling, *IEEE Trans. Image Process.* 25 (2) (2016) 818–828, <http://dx.doi.org/10.1109/TIP.2015.2509427>.
- [30] F. Mamalet, C. Garcia, Simplifying ConvNets for fast learning, in: *International Conference on Artificial Neural Networks*, 2012, URL: <https://api.semanticscholar.org/CorpusID:17018486>.